JGR Oceans

Correspondence to:
F. M. Bingham,
binghamf@uncw.edu

Seasonal and Interannual Variability of the Subtropical South Indian Ocean Sea Surface Salinity Maximum

F. M. Bingham[1], S. K. Brodnitz[1], and A. L. Gordon[2]

[1]Center for Marine Science, University of North Carolina Wilmington, Wilmington, NC, USA, [2]Lamont Doherty Earth Observatory, Columbia University, Palisades, NY, USA

Abstract The sea surface salinity (SSS) maximum of the South Indian Ocean (the SISSS-max) is a high-salinity feature centered at 30°S, 90°E, near the center of the South Indian subtropical gyre. It is located poleward of a region of strong evaporation and weak precipitation. Using several different satellites and in situ data sets, we track changes in this feature since the early 2000s. The centroid of the SISSS-max moves seasonally north and south, furthest north in late winter and farthest south in late summer. Interannually, the SISSS-max has moved on a northeast-southwest path about 1,500 km in length. The size and maximum SSS of the feature vary in tandem with this motion. It gets larger (smaller) and saltier (fresher) as it moves to the northeast (southwest) closer to (further from) the area of strongest surface freshwater flux. The area of the SISSS-max almost doubles from its smallest to largest extent. It was maximum in area in 2006, decreased steadily until it reached a minimum in 2013, and then increased again. The seasonal variability of the SISSS-max is controlled by the changes that occur on its poleward, or southern, side, whereas interannual variability is controlled by changes on its equatorward side. The variations in the SISSS-max are a complex dance between changes in evaporation, precipitation, wind forcing, gyre-scale ocean circulation, and downward Ekman pumping. Its motion correlated with SSS changes throughout the South Indian Ocean and may be an indicator of changes in the basin's subtropical circulation.

Plain Language Summary The ocean surface is saltiest in the mid-latitude subtropics where evaporation is strong and precipitation is weak. Each ocean basin has such a region, centered 20°–30° from the equator. These regions are sensitive indicators of a balance between the effects of the wind, evaporation, precipitation, and ocean currents. In this study, we focus on this salty region of the South Indian Ocean. It is centered around 30°S, 90°E, west of the coast of Australia. We have found variations in the size, saltiness, and position of the feature. It shifts over a northeast-southwest path on a year-to-year basis and gets saltier and fresher at the same time. Our conclusion is that this is largely a result of changes in the wind field and the shape and strength of the underlying ocean subtropical gyre. The motion we see is synchronized with similar motion of the analogs feature in the South Pacific, bringing up the likelihood of more global processes controlling both features.

1. Introduction

In five of the world's major ocean basins, there is an area of the subtropical ocean characterized by a horizontal maximum of sea surface salinity (SSS), situated typically around 25° latitude (Gordon et al., 2015). The classical view of these features (Bingham et al., 2019, 2014; Gordon & Giulivi, 2014; Katsura et al., 2013; Worthington, 1976; L. Zhang & Qu, 2014) has them being produced as a result of convergent Ekman transport underneath areas where evaporation greatly exceeds precipitation. At the latitude of the SSS maximum (the "SSS-max"), there is Ekman convergence and subduction as very salty water is incorporated into the interior circulation of the equatorward part of the subtropical gyre (Schmitt & Blair, 2015). These areas play a prominent role in the shallow overturning circulation (Gu & Philander, 1997; Kolodziejczyk & Gaillard, 2012; McCreary & Lu, 1994; Nonaka & Sasaki, 2007) which carries that salty water toward the equator, where it upwells and returns at the surface. SSS-max areas are closely associated with a strong excess of evaporation over precipitation (*E-P*), generally the strongest values in the global ocean (Schanze et al., 2010). Thus, variability in the SSS maxima may be an indicator of changes in the global water cycle, or the magnitude of transfer of water from ocean to atmosphere. It may also indicate variability in internal ocean processes that are less well understood.
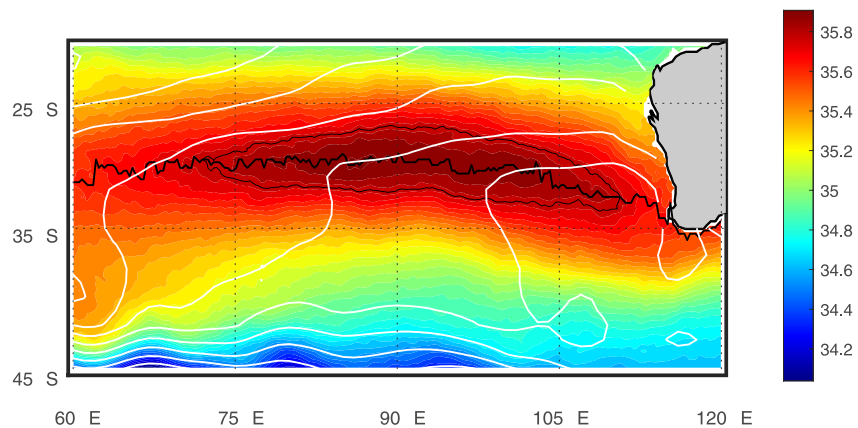
Figure 1. Mean sea surface salinity (SSS) (unitless practical salinity) for the 2010–2020 period in the South Indian Ocean from SMOS LOCEAN data. Color scale is at right. The thin black contour line marks SSS of 35.772 (a value used by Gordon et al., 2015). The wiggly black line going from west to east is the latitude of maximum SSS at each longitude. White contour lines are mean dynamic height relative to 2,000 m from EN4 data, with contour intervals at 0.1 dyn-m.

These SSS-max areas have been studied extensively in the Northern Hemisphere, especially in the North Atlantic (Lindstrom et al., 2015 and references therein), but have been less well characterized in the Southern Hemsiphere. With the advent of satellite measurement of SSS (Berger et al., 2002; Lagerloef et al., 2008; Vinogradova et al., 2019), we can begin to understand how these areas move and change. There are suggestions that SSS in these areas may be increasing globally (Boyer et al., 2005; Durack & Wijffels, 2010; Hosoda et al., 2009; Terray et al., 2012; Yu et al., 2020) as the hydrologic cycle accelerates on a warming planet.

In the effort to understand the dynamics and variability of these features, we focus here on the SSS-max in the South Indian Ocean (SIO; the "SISSS-max") and its location within the greater SIO and atmospheric circulation. The SISSS-max is a much more elongated feature than in other ocean basins. The center is the farthest poleward of all the ocean basins (Gordon et al., 2015) at approximately (30°S, 90°E). Gordon et al. (2015) surmised that this is due to the Australia-Asian monsoon that pushes the intertropical convergence zone into the Southern Hemisphere, and to the injection of freshwater into the eastern Indian Ocean from the Bay of Bengal and through the Maritime Continent. The SSS of the feature does not vary much over the breadth of the SIO (Figure 1).

The main previous study of the SISSS-max is that of Wang et al. (2020—henceforth "W20"). That study divided the SISSS-max into three separate features, one in the east just off of Australia, one in the center of the basin, and a third in the western part of the basin near Africa. In the average picture of Figure 1, we do not detect an isolated SSS-max close to Australia and do not look as far west as the coast of Africa, but we focus on what W20 call the central maximum. It stretches from about 70°E to 110°E and has SSS which reaches about 35.9 on average. The central maximum region identified by W20 starts at 90°E and stretches westward to 60°E, encompassing about half of the region identified in Figure 1. Our SISSS-max is a sort of combination of the eastern and central features of W20 as it encompasses the area shown in Figure 1.

The SISSS-max is embedded in the SIO surface circulation, which a number of studies have described. As a typical example, Reid (2003) plotted the mean geostrophic flow. At 30°S, where the SISSS-max is located, the geostrophic part of the flow is very weak. The paper plots a meandering "S-shaped" flow more or less to the north through the SISSS-max similar to that depicted in Figure 1. However, Reid notes that the surface circulation of the SIO is highly variable and that the type of averaging done was not ideal. Many studies of the SIO focus primarily on the tropical circulation, and have little to say about the flow in and around the SSS-max (e.g., Han & McCreary, 2001; Menezes et al., 2013; Molinari et al., 1990; Momin et al., 2015). Other studies of the subtropical SIO at the latitude of the SISSS-max come to much the same conclusion as Reid (2003), indicating weak flows at the surface, vaguely in the northward direction (W20; Divakaran & Brassington, 2011; Menezes et al., 2014; Palastanga et al., 2007; Phillips et al., 2021; Schott et al., 2002, 2009; Siedler et al., 2006; Stramma & Lutjeharms, 1997). Maes et al. (2018), using an eddy-resolving model, identify an area of surface convergence in the SIO centered at (30°S, 94°E). They also describe how the water from the region of the SISSS-max spreads from the South Indian into the South Pacific, perhaps leading to the formation of the secondary SSS-max in the western part of that basin (Gordon et al., 2015).

Below the surface, however, flows are better defined and more like what one might expect. At 200 db, Reid's (2003) mean flow turns by 90° relative to the surface and moves toward the northwest in a manner similar to what we might expect of a south equatorial current as the return limb of a subtropical gyre. This is similar to what we find in other ocean basins (e.g., Bingham et al., 2019; Dohan et al., 2015), and agrees with the sense of the wind-driven Sverdrup transport (Menezes et al., 2014; Schott et al., 2002). This northwestward-flowing interior circulation, however, does not seem to be associated with northwestward transport of salt. There is little sign of a distinct equatorward-westward spreading subsurface salt tongue (Han & McCreary, 2001) as is found in the North Atlantic (Schmitt & Blair, 2015), North Pacific (Katsura et al., 2013) or South Pacific (Kessler, 1999). Instead, the interior salinity distribution of the SIO is dominated by the low-latitude input of freshwater from the Pacific, via the straits and passages of the Maritime Continent (Han & McCreary, 2001).

In contrast to the lack of well-defined surface circulation within the SISSS-max, areas to the north and south have distinct flow features. To the south, the Antarctic Circumpolar Current (ACC) flows strongly to the east and also slants southward. This is visible in Figure 1 as a strong SSS front at 40°–45°S with closely spaced dynamic height contours (e.g., W20; Stramma & Lutjeharms, 1997). To the north, a current known as the South Indian Countercurrent (SICC) flows to the east in a highly variable banded pattern, with the southernmost band at around 25°S (Menezes et al., 2014, 2016; Palastanga et al., 2007; Siedler et al., 2006; W20). Again this is visible in the dynamic height field of Figure 1. In a contrasting view, Peng et al. (2015), using surface drifter data, do not show much of an SICC, except possibly in December and January. The area in the vicinity of the SISSS-max has relatively weak surface currents and mean and eddy kinetic energy. It is one of strong convergence as indicated by the way that drifters congregate at the very center of the SISSS-max (see their Figure 3).

The SISSS-max is the location of a minimum in mean wind stress (W20—their Figure 2c). It is tucked between southeasterly trade winds, which reach down to around 25°S, and westerlies which come as far north as 35°S. It has positive wind stress curl throughout, indicating a prevalence of downward Ekman pumping (Qu et al., 2019). The wind stress pattern is relatively steady throughout the seasons in a climatological sense (Schott et al., 2002). As a result of this minimum of wind stress, the surface circulation appears to converge directly at the latitude of the SISSS-max (Peng et al., 2015; Schott et al., 2002). This is in contrast to the all other ocean basins with SSS-maxima, where Ekman transport is poleward through the SSS-max (Gordon et al., 2015). The SIO has a larger eddy kinetic energy than the other Southern Hemisphere ocean basins, and as a result has a large eddy flux of salt, and the SISSS-max is also a maximum of convergence of salt flux (Qu et al., 2019). Thus, horizontal eddy flux of salt plays a larger role in the SIO than in other ocean basins.

W20 give a basic description of the SISSS-max. It is situated well to the south of the maximum of surface freshwater forcing which is around 10°–20°S. SSS within their central maximum has a seasonal cycle, with the highest value in April, that is, fall. They computed budgets for the eastern, central, and western SSS-maxima, both seasonally and interannually (2011–2015). For the central maximum, defined as a box with limits (35°–28°S, 60°–100°E), the budget was not closed in either case. The SSS tendency fluctuated strongly, but was not matched by a surface forcing, advection or vertical entrainment term. The tendency computed from satellite (Aquarius) data is very different from that computed from Argo data. The magnitude of tendency variability—it fluctuates on a scale of approximately ± 0.04 months^{-1}—is similar to other ocean basins (e.g., Dong et al., 2015; Katsura et al., 2013).

In this paper, we expand on the work of W20, to better define the seasonal cycle, and look at longer-term trends in the location and scope of the central SISSS-max. We relate the SISSS-max to the surface forcing and underlying subtropical gyre, in light of the results summarized above.

2. Data and Methods

Gordon et al. (2015) delineated the SISSS-max using the 35.772 isohaline at the surface, a convention we adopt here (Figure 1). This threshold isohaline value is derived from the MIMOC (Monthly Isopycnal/Mixed layer Ocean Climatology; Schmidtko et al., 2013) data set. We compute the area with this value of SSS or higher and the location of the centroid of this area in order to quantify the variability. We also compute and display values of surface flux in the region.

2.1. Data

See Acknowledgments section for details on version number and data access for all data sets used.

Table 1
Names, Spatial Grid Size and Dates for Sea Surface Salinity Data Sets Used

Data set name	Spatial grid size	Dates	Color in Figures 3–5
SMOS LOCEAN	0.25°	2010–December 2020	Yellow and black
SMOS BEC	0.25°	2010–December 2020	Red
SMAP JPL	0.25°	2015–December 2020	Green
SMAP RSS	0.25°	2015–December 2020	Black dashed
Aquarius	1°	2011–2015	Green
CCI—composite	0.25°	2010–2018	Black solid
EN4—in situ	1°	2004[a] to December 2020	Blue
RG—in situ	1°	2004[a] to December 2020	Cyan

Note. Colors in right columns refer to lines in Figures 3–5.

[a]EN4 and RG data go further back, but we chose to start in 2004.

There are several SSS data sets displayed, Two SMOS, two SMAP, one Aquarius, one L4 composite, and one in situ gridded (Table 1). All SSS data sets where retrieved from the source either as monthly averages, or averaged monthly after retrieval. The in situ data used are the EN4 data set of Good et al. (2013), and the Roemmich and Gilson (2009) data set (the "RG" data).

A few other data sets are used. The EN4 data, mentioned above, has a subsurface component, from which we compute dynamic height relative to 2,000 m depth.

Ekman transport data are sourced from NOAA's Environmental Research Division, and derived from the wind fields archived by the Fleet Numerical Meteorology and Oceanography Center. The product is called "FNMOC Wind and Ekman Transport Data, 360×180, Monthly, from 6 hr Pressure."

Freshwater forcing is defined as follows:

$$FWF = S_0 \frac{E - P}{h} \tag{1}$$

where S_0 is a constant, set to 35, E is evaporation, P precipitation, and h the mixed-layer depth. Evaporation data are monthly averages sourced from the OAFlux data set of Yu and Weller (2007). Precipitation are monthly values from IMERG (Integrated Multi-satellitE Retrievals for GPM; Skofronick-Jackson et al., 2017). Evaporation and precipitation data are interpolated onto a $1° \times 1°$ grid. We used a monthly climatological 1° mixed-layer depth product from MIMOC (Schmidtko et al., 2013). This product computes the mixed-layer depth following the method of Holte and Talley (2009). We tried some other non-climatological mixed-layer products and found them to be not useful for our purposes.

2.2. Methods

The area of the SISSS-max is defined here as the area with SSS higher than the threshold in the central SIO (60°–120°E, 20°–45°S). The meridional (zonal) centroid is the latitude (longitude) that half of the area is to the north (east) of in the central SIO. The meridional northern (southern) limit is the latitude that 95% of the area with SSS higher than the threshold is south (north) of. Similar definitions apply for the east/west limits of the feature. This calculation was done monthly.

We note here that there is a close relationship between average SSS (or maximum SSS) within the threshold isohaline and area. That is, when the area within the threshold isohaline is large the water within it is also salty as can be seen in Figure 2. This close relationship holds better for small values of area and gets more scattered as the area gets larger. What Figure 2 shows is that the isohaline area in the SIO is mainly a measure of how salty the water within the SSS-max is, both on a monthly and a yearly basis. On both monthly and yearly time scales the two are significantly correlated. This conclusion may seem self-evident, but it is worth confirming nonetheless.

3. Results

The area of SSS greater than 35.772 (Figure 3) shows a range of values and changes among the different products, which gives a sense of the uncertainty in the calculation. For the SMAP JPL product, the area appears to nearly quadruple between 2015 and 2020 from 0.5 to 2.0×10^6 km². The BEC product shows an increase, but not to the same degree, from about 1.5 to 2.5×10^6 km². The EN4 and SIO data have a maximum in 2017–2018, but generally increase from 2010 to 2020. The LOCEAN product has more variation than any of the others, and tends to have larger values, but with a strong decrease from 2012 to 2020. The Aquarius, CCI, and RSS SMAP products do not show much change over the time period depicted. There is seasonal variability in the different products too, with maximum SSS in summer (January–March) and minimum in winter (July–August; Gordon et al., 2015). This seasonality is more difficult to detect in the CCI, LOCEAN, and BEC products, but quite apparent in the EN4, SIO, Aquarius, and the two SMAP products.

The different data sets are much more consistent when it comes to showing the changing position of the feature. In the north-south direction (Figure 4) the data sets have consistent interannual and seasonal changes. The
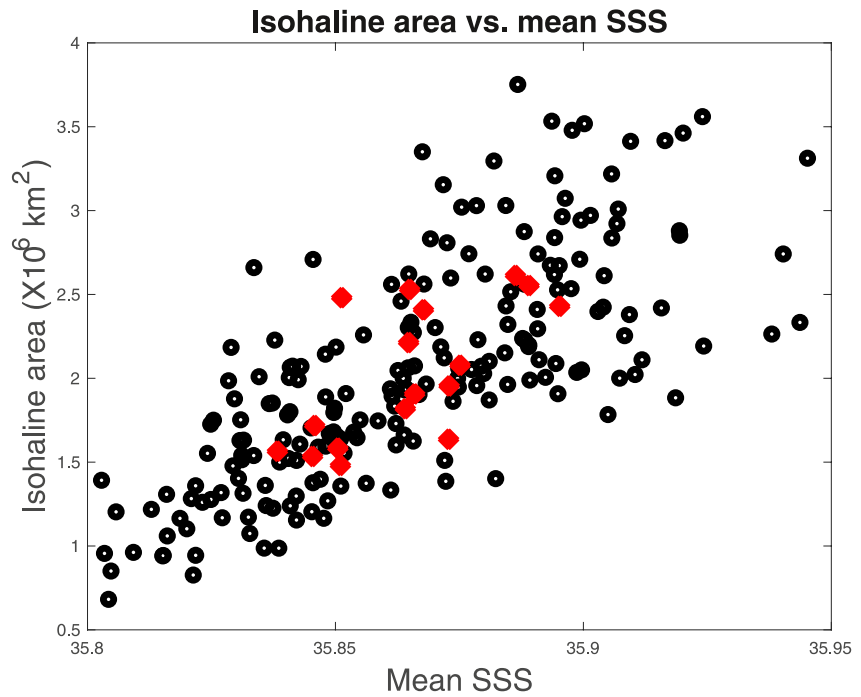
Figure 2. Mean sea surface salinity (SSS) computed within the 35.772 isohaline versus area with SSS >35.772 from EN4. Black symbols are monthly (areas are the same data displayed in Figure 6). Red symbols are yearly averages (areas are the same data displayed in Figure 8).
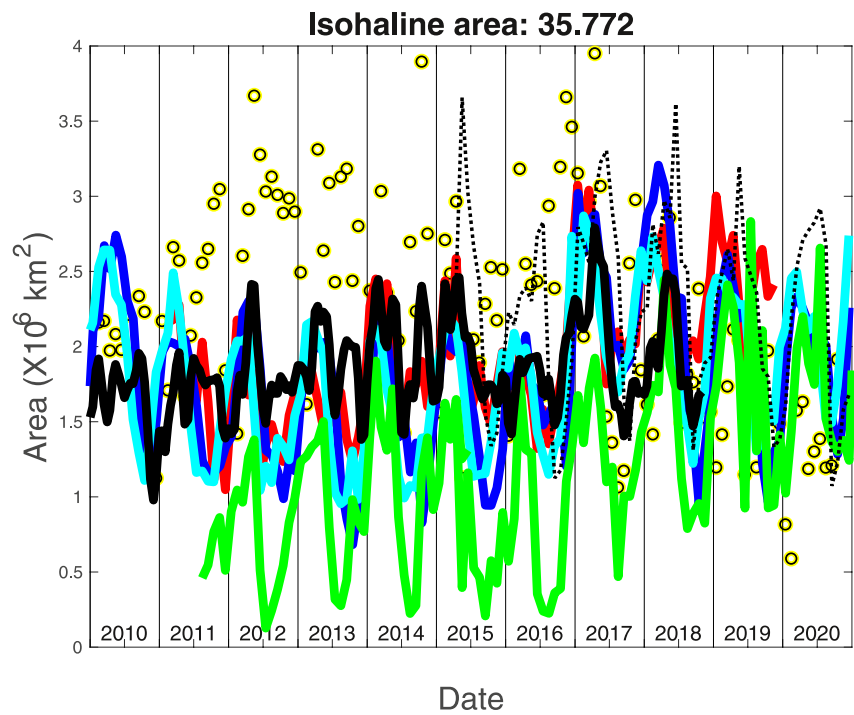

Figure 3. Area with sea surface salinity greater than 35.772 as a function of time with units of 10^6 km². The different colors represent different satellite and other products, with a color key in Figure 4 and Table 1. Note, the JPL SMAP and Aquarius products are the same color (green) and overlap by a couple of months in early 2015.
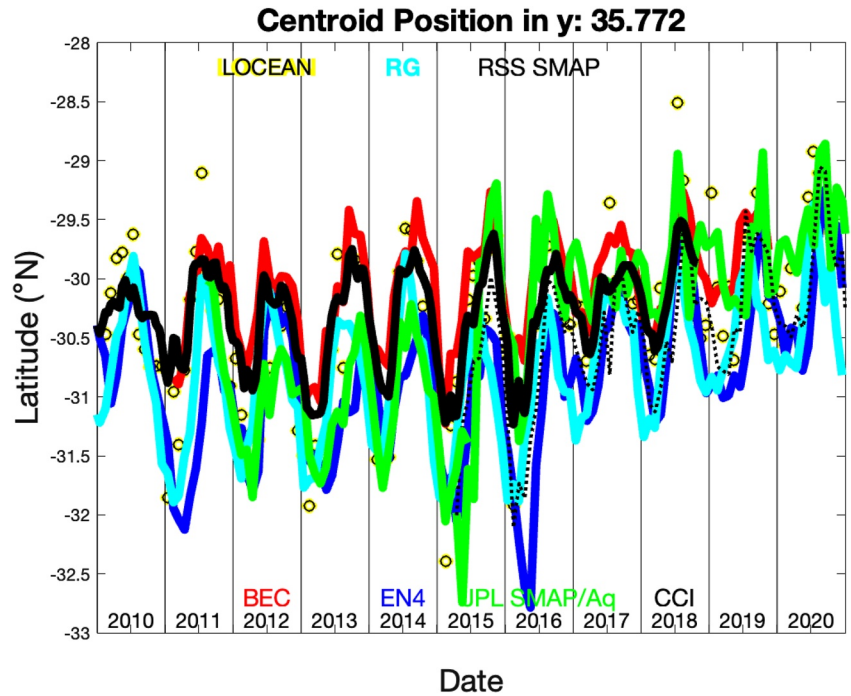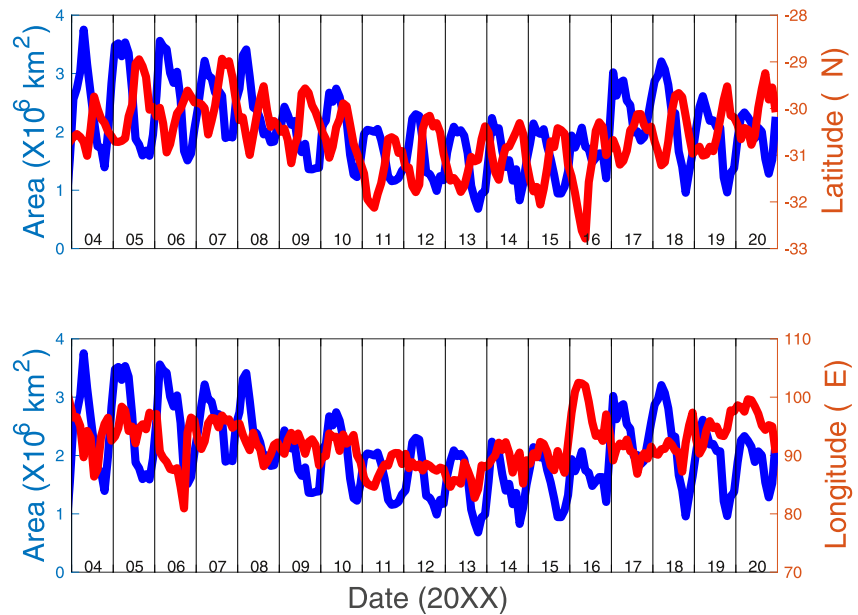
Figure 4. Latitude position of the centroid of the 35.772 isohaline in the South Indian Ocean. The different data set are keyed to colors as shown at the bottom of the figure and in Table 1. The RSS-SMAP curve is dashed. Note, the JPL SMAP and Aquarius products are the same color (green) and overlap by a couple of months in 2015.
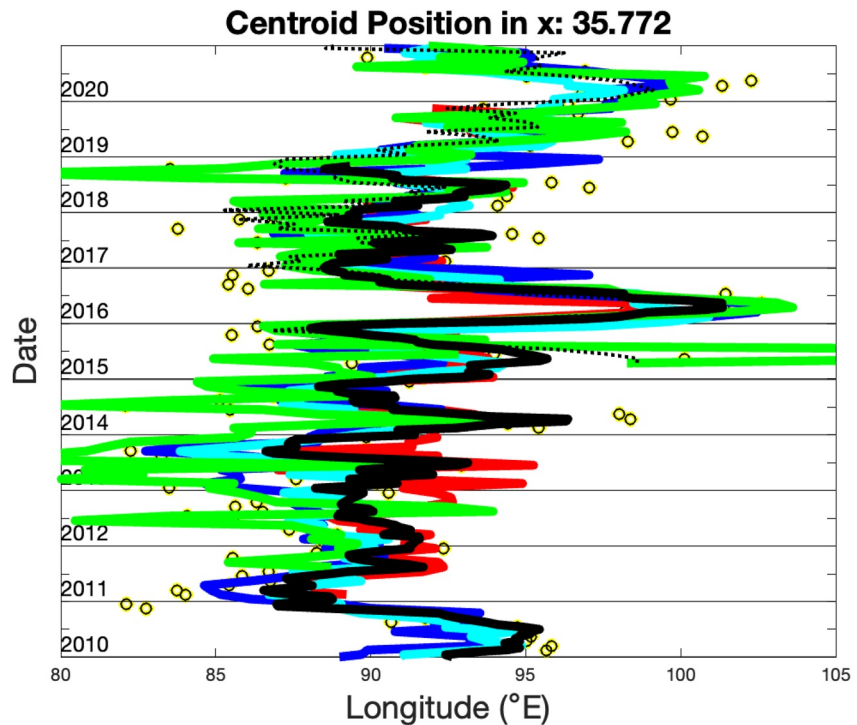
Figure 5. Longitude position of the centroid of the 35.772 isohaline in the South Indian Ocean. The different data set are keyed to colors as shown in Figure 4 and Table 1. The RSS-SMAP curve is dashed. Note, the JPL SMAP and Aquarius products are the same color (green) and overlap by a couple of months in 2015.

Figure 6. From EN4 data. Top panel: Blue curve/left axis, area with SSS >35.772. Red curve/right axis, latitude position of the centroid. Lower panel: Blue curve/left axis, area with SSS >35.772, same as the top panel. Red curve/right axis, longitude position of the centroid. Blue curves are the same in each panel.

SISSS-max moved steadily equatorward between 2010–2011 and 2020, with total motion of 0.5°–1°. This is apparent in every data set, but to different degrees. The EN4 data set starts out with the centroid at 30.5°–31°S in 2010–2011, and it moves northward to 29.5°S in 2020, with a large excursion southward in 2015. There is significant seasonality as well in this north-south motion. The feature is furthest south in summer and north in winter, as seen consistently in all the data sets. The amplitude of the seasonal north-south motion is 1°–1.5°.

The longitude position of the centroid (Figure 5) is more variable within products, but again the different products are relatively consistent with each other. Between about 2011 and 2020, the position of the centroid moves significantly eastward, from about 87°E to about 99°E, a distance of over 1,000 km. There are large excursions during this time. In 2016, the feature moves far eastward, past 100°E in some data sets. In 2013, the feature moved far westward, to 80°–85°E. This westward motion is also detected in 2012, 2014, and 2018, but only by the JPL SMAP and Aquarius products. Seasonal variability in the longitude position of the SISSS-max does not stand out in this display. It may be present but overshadowed by longer-term variability.

The EN4 in situ data set gives an idea of the trends in position and area over a longer time scale (Figure 6), and a number of items can be noticed. The seasonal cycle in area changes in amplitude. From 2004 to 2008, the range of the seasonal cycle is about 2×10^6 km^2. After that, there appears to be some kind of regime shift, where the range decreases to about 1×10^6 km^2 and the area decreases, until about 2013. After that, the area increases again, and the range does as well. The latitude shifts in tandem with the area. It starts out at close to 30°S. It then shifts southward for several years until about 2013, when it reaches a southward excursion of about 31.5°S. After that it again moves northward. The latitude has a seasonal cycle with a range of 1°–1.5°, but it remains about the same amplitude throughout. The longitude position (lower panel) does not have a visible seasonal cycle, but does have interannual variability in sync with the area and latitude. The feature moves farthest west in 2013 to about 85°E. Before and after that it is further east as far as 100°E in 2016.

Putting the east-west and north-south motion together into an annual average (Figure 7), we see that the SISSS-max shifts substantially along an almost linear southwest-northeast path. The southwestern limit was reached in about 2013 (green contour) and the northeast limit in 2020 (black and yellow contour). The year 2016 was an exception: The SISSS-max was farther east, but shifted to the south as well. This is due to one event that occurred in March–April of that year as can be seen in Figure 6. The size is also correlated with these motions. As the feature moves to the northeast it gets larger, and smaller when it moves to the southwest.
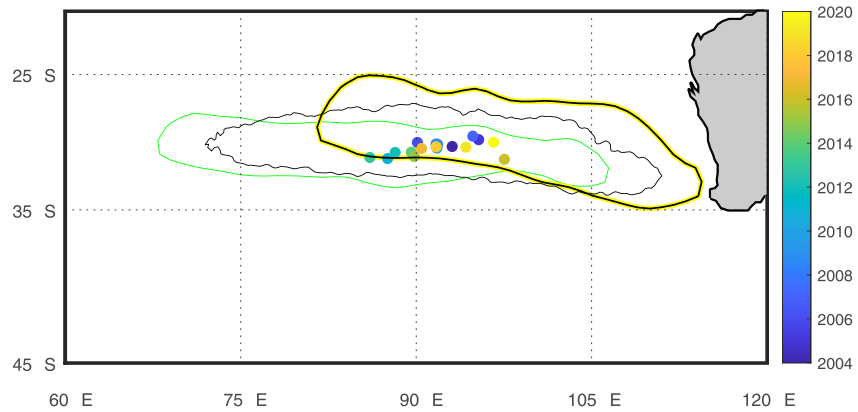
Figure 7. Annual-average centroid position from EN4 data. The symbols are color-coded by year with the scale at right. The light black line is the annual average 35.772 contour from Figure 1. The green line is the same contour averaged for 2013, when the area is minimum and the feature is far to the southwest. The yellow and black line is for the year 2020, when the area is large and the feature is far to the northeast.

The yearly average area (Figure 8) shows large changes in area over time. The area ranges from a high of 2.6×10^6 km^2 in 2006 down to a low of just over 1.4×10^6 km^2 in 2013, a decrease by a factor of almost 2 in 7 yr. The area abruptly increased again to another maximum in 2017 and another sharp decrease. The overall picture is of a feature with large coherent interannual changes. Putting this change in area together with the motion in Figures 4–7, the SISSS-max gets smaller as it moves to the southwest and larger as it moves northeast.

We can learn more about what causes the observed variability of the SISSS-max by looking at the limits of the feature (Figure 9). As noted before, the SISSS-max moves north and south over the course of the year. It is clear from Figure 9a that most of that change is a result of the motion of the poleward boundary, which has a large seasonal cycle of range about 3°. This seasonal motion occurs every year, though the size of it changes, being larger in some years (e.g., 2016) and smaller in others (e.g., 2004). By contrast, the interannual variability of the SISSS-max position is mainly determined by the equatorward boundary. This has no discernible seasonal cycle, but large interannual changes. It moves from close to 25°S in 2005, down to about 29°S in 2013. It is hard to
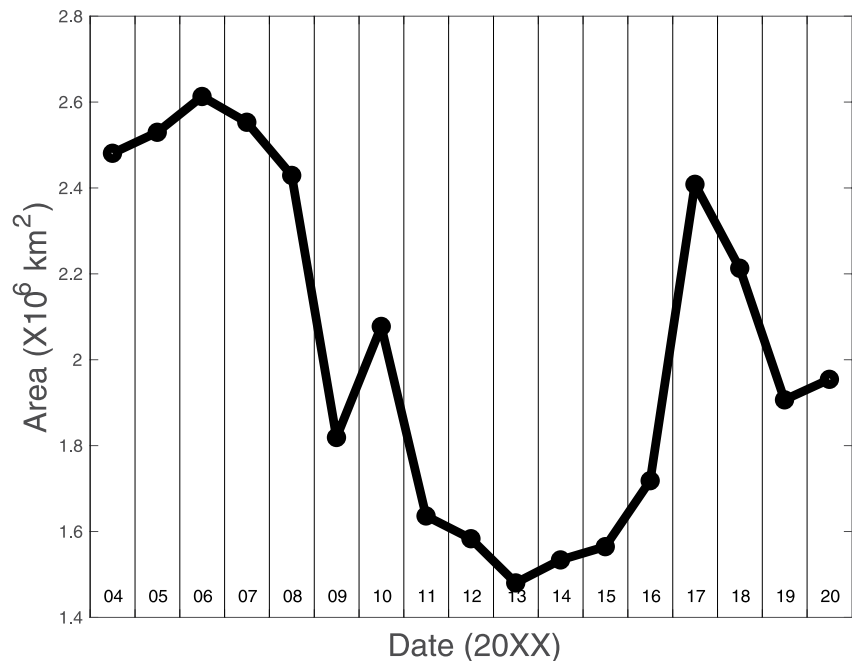
Figure 8. Annual average area of SSS >35.772 in the South Indian Ocean from EN4 data.
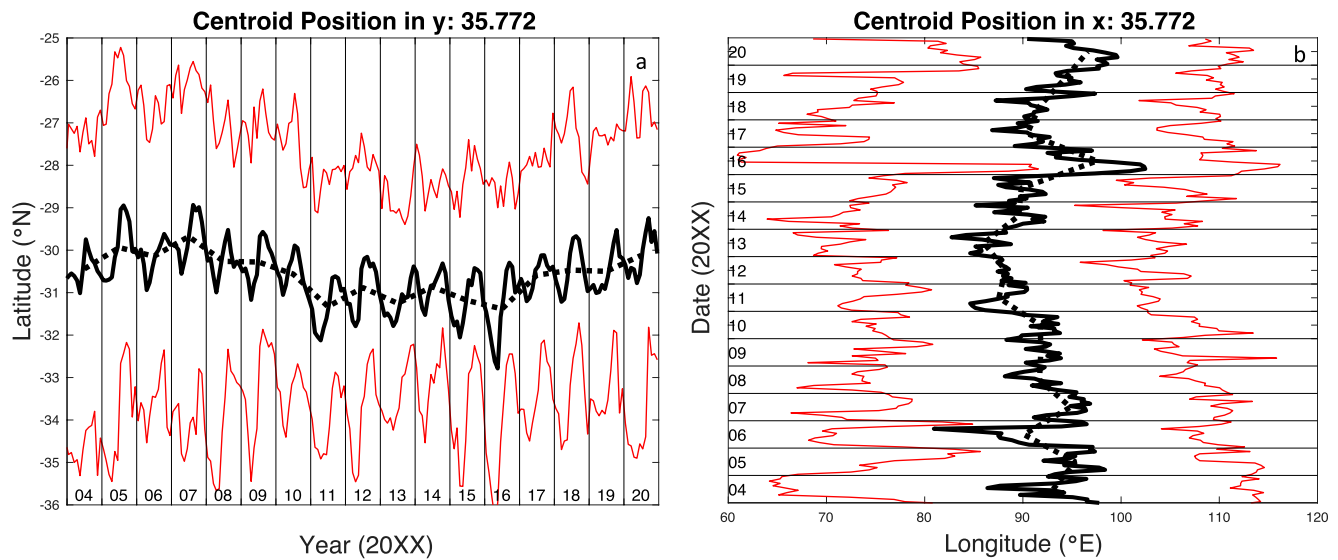
Figure 9. From EN4 data. (a) Black curves: Latitude of the centroid of the SISSS-max. Solid curve is monthly, dashed curve is the yearly average. This is the same as the red curve in Figure 5 upper panel. Upper (lower) red curve: latitude of the 95th percentile of area. That is, 95% of the area with SSS >35.772 is south (north) of this latitude. (b) As in panel (a) but for the longitude of the centroid and with time on the *y*-axis.

detect any seasonal cycle in the east-west motion of the SISSS-max (Figure 9b). It has interannual variability as discussed above, but i.e., not dominated by either the eastern or western side. The western side of the feature appears more highly variable in position then the eastern side.

One can see how the SISSS-max fits into the larger scale variability of the SIO on an interannual time scale by looking at the correlation between the area (Figure 8) and the SSS over the larger SIO (Figure 10). The pattern is quite striking. North of the SISSS-max, the correlation is positive, with values as high as 0.8. South of the SISSS-max, the pattern is opposite, negative correlations with some very low values. The boundary, with near-zero correlation, runs along the northern edge of the SISSS-max. This explains the northeast-southwest translation shown in Figure 7. As the SISSS-max moves to the northeast, the area gets larger and SSS within the feature increases. As it moves to the southwest, the area gets smaller and the SSS decreases. The highest positive correlations are near the west coast of Australia. The SISSS-max moves closer to there as it gets saltier and larger as seen in Figure 7. This picture puts the SISSS-max within a large-scale see-saw pattern in the SIO, high SSS in the lower latitudes corresponding with low SSS in higher latitudes, and vice versa. It should be noted that the picture in Figure 10 is based on only 17 yr of data, so does not have a high degree of statistical confidence.
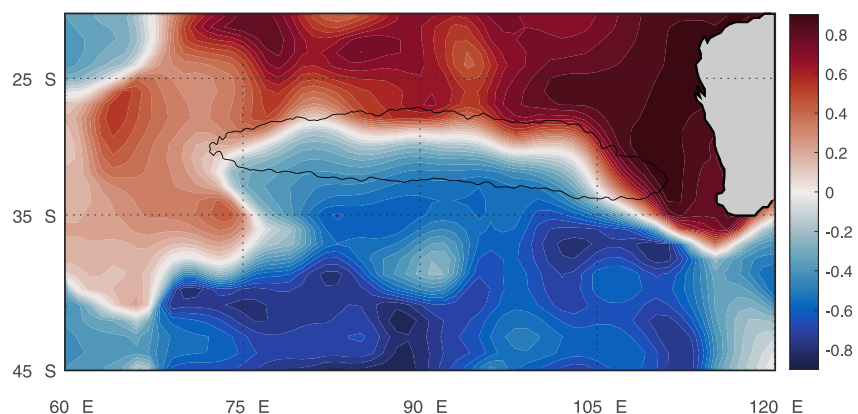
Figure 10. Unitless correlation between annual average area (Figure 8) and annual-average sea surface salinity at each location in the South Indian Ocean. Data are from the EN4 data set over the 2004–2020 time period. Thin black line is the mean 35.772 isohaline as in Figure 1.
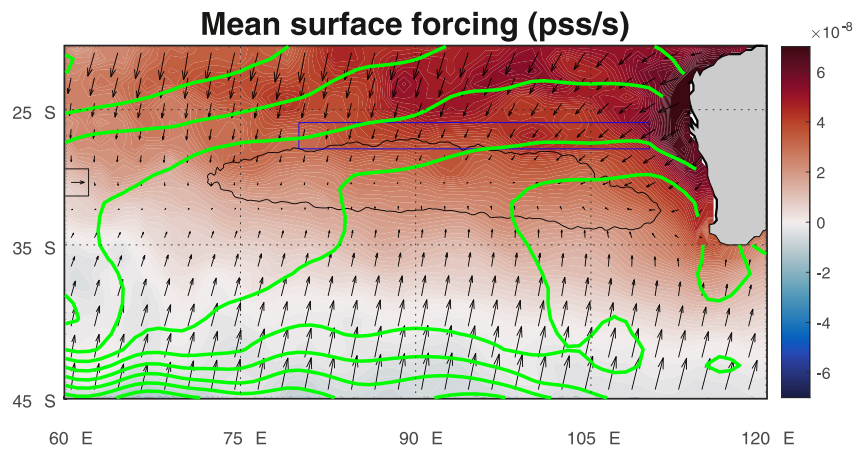
Figure 11. Averages over 2004–2020. Colors: freshwater forcing (see Equation 1). Color scale is at right, with units of pss/s. Positive (red) values indicate freshwater forcing out of the ocean, that is, net evaporation. Green contour lines: dynamic height at the surface relative to 2,000 m from EN4 data, with units of dyn-m and a contour interval of 0.1, the same field as displayed in Figure 1. Arrows: mean Ekman transport from FNMOC. A scale arrow is displayed at the left in a box with magnitude 1,000 m² s⁻¹. Light black line is the SSS = 35.772 contour as in Figure 1. Blue box (80°–110°E, 26°–28°S) is where the average in Figure 13 is taken from.

As discussed above, the SISSS-max is embedded in the SIO circulation, and is impacted by winds and freshwater forcing at the surface. In the (2010–2020) mean, the SISSS-max sits within a region that is evaporation-dominated (red area in Figure 11). The boundary between evaporation and precipitation-dominated regions crosses the study area diagonally from (27°S, 60°E) to (42°S, 120°E). The SISSS-max is to the northeast of this delineation, similar to the South Pacific (Bingham et al., 2019). The feature is located to the southwest of where the freshwater forcing is most strongly positive, which in Figure 11 is 20°–25°S (see also Gordon et al., 2015, their Figure 1b). Again, this placement is similar to that of the SSS-max in the South Pacific. As discussed in the introduction, the underlying geostrophic circulation is very weak, especially poleward of the SISSS-max. It is more or less northward from the ACC at 40°–45°S to the SISSS-max. At a latitude of about 30°S, in the middle of the SISSS-max, the flow strengthens and takes a right-hand turn toward the Australian continent.

The wind systems over the SIO drive much of the surface circulation via Ekman transport as shown in Figure 11. The SISSS-max is situated in an area of weak Ekman flow and large-scale convergence. It seems clear from this figure that the basic placement of the feature is determined by the winds and associated surface circulation.

The wind field that impacts the SISSS-max varies with time. The most relevant variation occurs near the coast of Australia at (30°S, 110°E), with minimum seasonal speed in winter (Figure 12). The seasonal aspect of this variability has the SIO subtropical high the results of which are depicted in Figure 11 getting stronger and weaker at this location, or, alternatively, moving equatorward and poleward. The high is furthest equatorward in winter, and thus winds are weak. This north-south shifting of the winds may relate to the seasonal changes in the SISSS-max at its poleward edge. Perhaps when the winds are strongest there in summer, evaporation increases and so does the SSS. The interannual variability at this location indicates weak winds in the 2011–2014 time period, coincident with the minimum in area shown in Figure 8.

Given that the SISSS-max is closely linked to the surface forcing, it would be logical to conclude that variability of the forcing in the area equatorward of the feature is related to the area or motion. However, this does not seem to be the case. *E-P* averaged within the box in Figure 11 is quite variable on short time scales, but relatively steady interannually (Figure 13). There is a small dip in 2018 due to three anomalous months at the end of the year, and perhaps a slight downward trend overall. Given this result, it seems variability of *E-P* just equatorward of the SISSS-max does not directly control SSS variability or the size or position of the feature.

As shown in Figure 11, the gyre-scale geostrophic flow beneath the SISSS-max is northeastward, more or less opposite to the Ekman component. The geostrophic flow across 27°S is indicated by the dynamic height between 80° and 110°E. The sea surface slopes generally downward from west to east, consistent with net northward motion. There is an O (20 cm) height difference from west to east (Figure 14). The gradient across the breadth
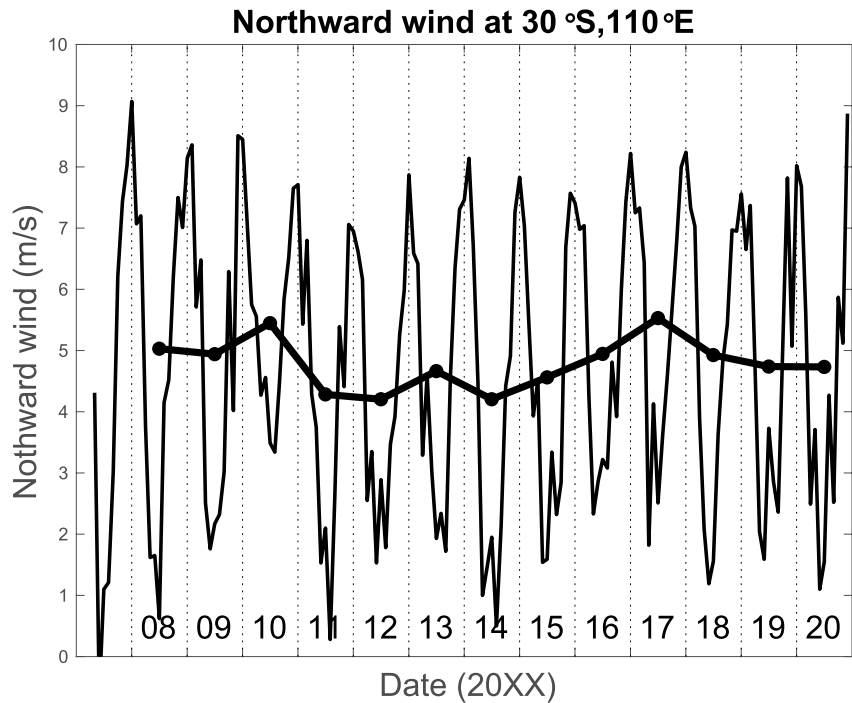
Figure 12. Northward wind at (30°S, 110°E). Variable black line is from monthly averages. Smoother black line with symbols is a yearly average.
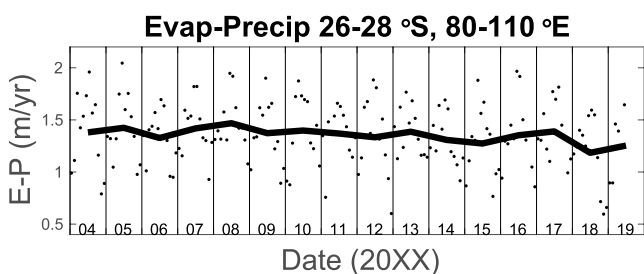
of the SISSS-max varies from year-to-year, but comes to a minimum in the years 2011–2015. This is especially notable in the longitude range of 95°–110°E, where there is a maximum of dynamic height during this period. These are the same years in which the area of the feature reached a minimum and it translated farthest to the southwest. Thus, the large-scale gyre flow may control, or is at least correlated with, the position and size of the SISSS-max.
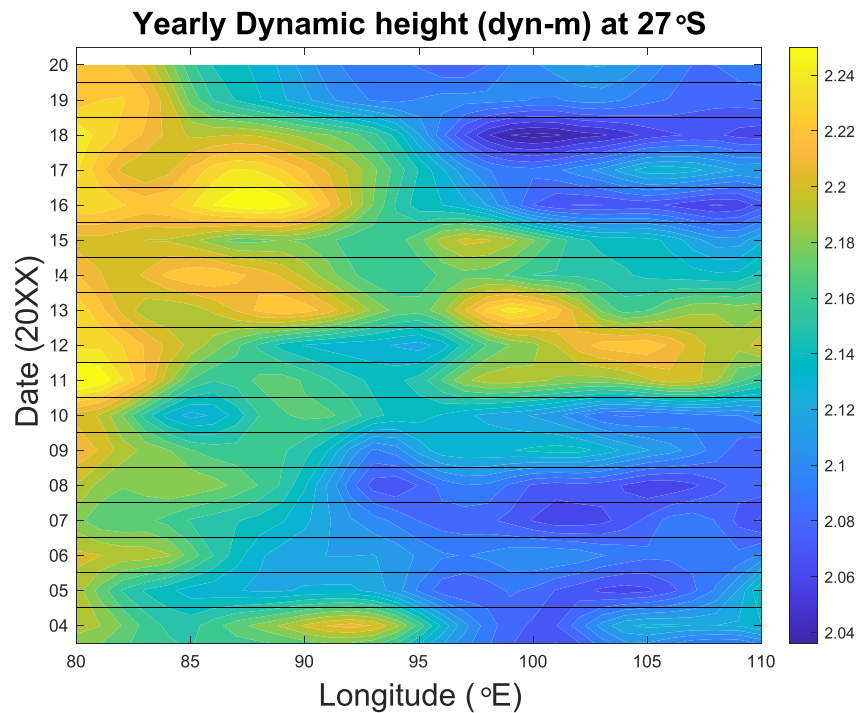
4. Discussion

The SIO SSS-max has been shown to vary on seasonal and interannual time scales in its position (Figures 4–7), size (Figures 3 and 6–8) and intensity (Figure 2). Its centroid moves in a distinct northeast-southwest track (Figures 6 and 7) for reasons that are still not entirely clear, but may relate to the balance between Ekman transport and the geostrophic flow of the subtropical gyre. The flow of the subtropical gyre tends to push the feature to the northeast, while Ekman transport pushes it to the southwest. The fact that the SISSS-max is situated slightly to the northeast of the minimum of the mean Ekman transport (Figure 11) bears this out. The apparent correlation between position and size/intensity makes sense. As the feature moves northeastward, it moves into an area more dominated by evaporation and thus gets saltier.

Figure 13. E-P (m/yr) averaged over the box shown in Figure 11. Black dots are monthly values. Black curve is yearly averages.

Advection is small within the SISSS-max relative to surrounding areas (not shown). This makes sense as the SSS gradient becomes small near the meridional peak of SSS - advection is the dot product of the velocity and SSS gradient. So a determining factor in the size, position, and intensity of the SISSS-max may be not so much the strength of evaporation at the center of the feature, but the evaporation imposed on the source waters as they flow toward it, and the amount of time that water spends underneath this strong evaporation while in transit (Bingham et al., 2014; D'Addezio & Bingham, 2014). However, this idea is not the subject of the current work. It

Figure 14. Yearly averaged dynamic height (in dyn-m) from EN4 data along 27°S as a function of time.

may be better to study the SSS-max in a Lagrangian framework, where we could understand the evolution of the source waters in their approach to the SSS-max.

We have not explicitly addressed the role of eddy advection of salt in the variability of the SISSS-max. Eddy processes may be more of a factor in the SIO than in other oceans due to elevated eddy kinetic energy, especially on the equatorward side. Qu et al. (2019) emphasize this point showing a large divergence of the salt flux centered at the SISSS-max. Johnson et al. (2016) also describe the importance of eddy over mean advection. Though the eddy flux may be important in the mean location of the SISSS-max, it is not clear how or if eddy processes may contribute to the variability of the position or size. Are there interannual changes in the strength of eddy advection?

The main seasonal variation in the SISSS-max is expansion and contraction on the poleward side (Figure 9a). There may be a role of seasonal variability in vertical entrainment in this. Vertical entrainment shifts from downwelling to upwelling and back again over the course of the year. Vertical processes are driven by the curl of the wind stress and the heaving of the base of the mixed layer. The prevailing winds (not shown) indicate that the mean zero in wind stress is found south of the SISSS-max, at about 35°S. Seasonal shifting in the strength and distribution of the wind stress curl may be the cause of the seasonality in vertical entrainment and thus the poleward edge of the SISSS-max (N. Zhang et al., 2016). Bingham et al. (2021) have shown that there is a strong seasonal cycle in the small-scale (<100 km) variance of SSS in the vicinity of the SISSS-max, with maximum in the fall season. This is likely due to seasonal variation of rainfall. How this might impact the expansion and contraction of the SISSS-max on its poleward side is still an open question.

The close relationship of the SISSS-max to the wind field is emphasized in Figures 11 and 12. Variability of the wind field can impact the SISSS-max in several different ways, through Ekman transport which advects water toward the feature, through Ekman convergence which determines the structure of the underlying subtropical gyre and also causes SSS-max water to subduct and enter the interior flow, and through changes in evaporation which is closely tied to wind speed. Future research can help sort out which of these is most important in helping to shape the structure of the SISSS-max.

The SISSS-max in the eastern Indian Ocean is also influenced by the input of low salinity water from its equatorward side. The surface layer and thermocline off the northwest coast of Australia has low salinity, mainly due to Indonesian Throughflow (ITF). This results in relatively high sea level that induces a north to south pressure

gradient off the west coast of Australia, driving the southward flowing Leeuwin Current (LC) (Gruenberg, 2021). The poleward flowing LC is an unusual subtropical gyre eastern boundary current, which in other oceans flows toward the equator. The north-south pressure gradient is more effective in sending low salinity water into the LC when the northward winds relax which truncates the eastern extension of the 35.772 isohaline.

Bingham et al. (2019) studied the SSS-max in the South Pacific in a similar way as we have done here, and found similar variability in the centroid. There was a minimum in area, but 1–2 yr before the one we have shown in this paper in the South Indian. The fact that the two SSS-maxima behave in similar ways suggests that their motion is a result of similar forces, or that one influences the other. In the South Pacific Bingham et al. (2019) suggested that the variability is linked to the Pacific Decadal Oscillation (PDO), and found significant correlation between the PDO index and the annul-average area. There was a minimum in PDO in 2009, and a minimum in SSS-max area in 2011. Thus, the SSS-max area in the South Pacific lags the PDO by ∼2 yr, and, by extension, the lag between PDO and SISSS-max area is ∼3–4 yr. Perhaps the increased delay in the SIO results from the fact that the SISSS-max is 5° poleward of that of the South Pacific. Another possibility is the role of the ITF in connecting the Pacific and Indian Ocean basins that adds a time delay in the Indian Ocean response relative to the Pacific. Regardless of the reason, the synchronicity of the motion of the centroid in the South Pacific and South Indian emphasizes the interconnectedness of the two ocean basins (Qu et al., 2019).

As stated above, the SISSS-max is the result of a delicate balance between a number of competing and complementary processes, northeastward motion due to the underlying subtropical geostrophic circulation, southwestward motion due to Ekman transport, vertical entrainment variability at the poleward edge, eddy advection in the region equatorward of the SISSS-max and a predominance of evaporation over precipitation which decreases toward the southwest. All of these have a role in determining the position, size, intensity and variability of the feature, which can change in response to changes in any of these processes. In order to understand the balance of forces affecting the interannual variability of the SISSS-max, one has to study not just the processes within it, but the variability of the source waters, the wind systems that drive Ekman transport and downwelling and the eddy transport on the equatorward side.

Data Availability Statement

Data used in this paper may be obtained from the following sources: SMOS LOCEAN V5: https://data.catds.fr/cecos-locean/Ocean_products/L3_DEBIAS_LOCEAN/L3_DEBIAS_LOCEAN_v5/debiasedSSS_09days_v5/; SMOS BEC: https://bec.icm.csic.es/ocean-global-sss/; SMAP JPL: https://doi.org/10.5067/SMP50-3TMCS; SMAP RSS: https://data.remss.com/smap/SSS/V05.0/FINAL/L3/monthly/; Aquarius: https://doi.org/10.5067/AQR50-3YMCE; CCI: https://doi.org/10.5285/9ef0ebf847564c2eabe62cac4899ec41; EN4: https://www.metoffice.gov.uk/hadobs/en4/download-en4-2-2.html; RG: http://sio-argo.ucsd.edu/RG_Climatology.html; OAFlux: https://oaflux.whoi.edu/data-access/; IMERG: https://gpm.nasa.gov/data/directory; MIMOC: https://www.pmel.noaa.gov/mimoc/; FNMOC Wind and Ekman Transport Data: https://coastwatch.pfeg.noaa.gov/erddap/griddap/erdlasFnWPr.html.

References

Berger, M., Camps, A., Font, J., Kerr, Y., Miller, J., Johannessen, J., et al. (2002). Measuring ocean salinity with ESA's SMOS mission. *ESA Bulletin*, *111*, 113–121.

Bingham, F. M., Brodnitz, S., Fournier, S., Ulfsax, K., Hayashi, A., & Zhang, H. (2021). Sea surface salinity subfootprint variability from a global high-resolution model. *Remote Sensing*, *13*(21), 4410. https://doi.org/10.3390/rs13214410

Bingham, F. M., Busecke, J. J. M., & Gordon, A. L. (2019). Variability of the South Pacific subtropical surface salinity maximum. *Journal of Geophysical Research: Oceans*, *124*(8), 6050–6066. https://doi.org/10.1029/2018JC014598

Bingham, F. M., Busecke, J., Gordon, A. L., Giulivi, C. F., & Li, Z. (2014). The North Atlantic subtropical surface salinity maximum as observed by Aquarius. *Journal of Geophysical Research: Oceans*, *119*(11), 7741–7755. https://doi.org/10.1002/2014JC009825

Boyer, T. P., Levitus, S., Antonov, J. I., Locarnini, R. A., & Garcia, H. E. (2005). Linear trends in salinity for the World Ocean, 1955–1998. *Geophysical Research Letters*, *32*(1), L01604. https://doi.org/10.1029/2004GL021791

D'Addezio, J. M., & Bingham, F. M. (2014). A subtropical North Atlantic regional atmospheric moisture budget. *Journal of Geophysical Research C: Oceans*, *119*(12), 8731–8748. https://doi.org/10.1002/2014JC010300

Divakaran, P., & Brassington, G. B. (2011). Arterial ocean circulation of the southeast Indian Ocean. *Geophysical Research Letters*, *38*(1). https://doi.org/10.1029/2010GL045574

Dohan, K., Kao, H.-Y., & Lagerloef, G. S. E. (2015). The freshwater balance over the North Atlantic SPURS domain from Aquarius satellite salinity, OSCAR satellite surface currents, and some simplified approaches. *Oceanography*, *28*(1), 86–95. https://doi.org/10.5670/oceanog.2015.07

Dong, S., Goni, G., & Lumpkin, R. (2015). Mixed-layer salinity budget in the SPURS region on seasonal to interannual time scales. *Oceanography*, *28*(1), 78–85. https://doi.org/10.5670/oceanog.2015.05

Durack, P. J., & Wijffels, S. (2010). Fifty-year trends in global ocean salinities and their relationship to broad-scale warming. *Journal of Climate*, *23*(16), 4342–4362. https://doi.org/10.1175/2010JCLI3377.4341

Good, S. A., Martin, M. J., & Rayner, N. A. (2013). EN4: Quality controlled ocean temperature and salinity profiles and monthly objective analyses with uncertainty estimates. *Journal of Geophysical Research: Oceans*, *118*(12), 6704–6716. https://doi.org/10.1002/2013JC009067

Gordon, A. L., & Giulivi, C. F. (2014). Ocean eddy freshwater flux convergence into the North Atlantic subtropics (Vol. *119*, pp. 3327–3335). https://doi.org/10.1002/2013JC009596

Gordon, A. L., Giulivi, C. F., Busecke, J., & Bingham, F. M. (2015). Differences among subtropical surface salinity patterns. *Oceanography*, *28*(1), 32–39. https://doi.org/10.5670/oceanog.2015.02

Gruenberg, L. K. (2021). *Indonesian throughflow heat transport, and spreading within the eastern tropical Indian Ocean (Ph.D. dissertation)*. Columbia University. https://doi.org/10.7916/d8-s7eg-ke09

Gu, D., & Philander, S. G. (1997). Interdecadal climate fluctuations that depend on exchanges between the tropics and extratropics. *Science*, *275*(5301), 805–807. https://doi.org/10.1126/science.275.5301.805

Han, W., & McCreary, J. P., Jr. (2001). Modeling salinity distributions in the Indian Ocean. *Journal of Geophysical Research: Oceans*, *106*(C1), 859–877. https://doi.org/10.1029/2000JC000316

Holte, J., & Talley, L. (2009). A new algorithm for finding mixed layer depths with applications to Argo data and subantarctic mode water formation. *Journal of Atmospheric and Oceanic Technology*, *26*(9), 1920–1939. https://doi.org/10.1175/2009JTECHO543.1

Hosoda, S., Suga, T., Shikama, N., & Mizuno, K. (2009). Global surface layer salinity change detected by Argo and its implication for hydrological cycle intensification. *Journal of Oceanography*, *65*(4), 579–586. https://doi.org/10.1007/s10872-009-0049-1

Johnson, B. K., Bryan, F. O., Grodsky, S. A., & Carton, J. A. (2016). Climatological annual cycle of the salinity budgets of the subtropical maxima. *Journal of Physical Oceanography*, *46*(10), 2981–2994. https://doi.org/10.1175/JPO-D-15-0202.1

Katsura, S., Oka, E., Qiu, B., & Schneider, N. (2013). Formation and subduction of North Pacific tropical water and their interannual variability. *Journal of Physical Oceanography*, *43*(11), 2400–2415. https://doi.org/10.1175/JPO-D-13-031.1

Kessler, W. S. (1999). Interannual variability of the subsurface high salinity tongue south of the equator at 165°E. *Journal of Physical Oceanography*, *29*(8), 2038–2049. https://doi.org/10.1175/1520-0485(1999)029<2038:IVOTSH>2.0.CO;2

Kolodziejczyk, N., & Gaillard, F. (2012). Observation of spiciness interannual variability in the Pacific pycnocline. *Journal of Geophysical Research: Oceans*, *117*(C12). https://doi.org/10.1029/2012JC008365

Lagerloef, G. S., Colomb, F. R., Le Vine, D., Wentz, F., Yueh, S., Ruf, C., et al. (2008). The Aquarius/SAC-D mission: Designed to meet the salinity remote-sensing challenge. *Oceanography*, *20*(1), 68–81. https://doi.org/10.5670/oceanog.2008.68

Lindstrom, E., Bryan, F., & Schmitt, R. (2015). SPURS: Salinity processes in the upper-ocean regional study. *Oceanography*, *28*(1), 14–19. https://doi.org/10.5670/oceanog.2015.01

Maes, C., Grima, N., Blanke, B., Martinez, E., Paviet-Salomon, T., & Huck, T. (2018). A surface "Superconvergence" pathway connecting the South Indian Ocean to the Subtropical South Pacific gyre. *Geophysical Research Letters*, *45*(4), 1915–1922. https://doi.org/10.1002/2017GL076366

McCreary, J., & Lu, P. (1994). On the interaction between the subtropical and equatorial ocean circulations: The subtropical cell. *Journal of Physical Oceanography*, *24*, 466–497.

Menezes, V. V., Phillips, H. E., Schiller, A., Bindoff, N. L., Domingues, C. M., & Vianna, M. L. (2014). South Indian countercurrent and associated fronts. *Journal of Geophysical Research: Oceans*, *119*(10), 6763–6791. https://doi.org/10.1002/2014JC010076

Menezes, V. V., Phillips, H. E., Schiller, A., Domingues, C. M., & Bindoff, N. L. (2013). Salinity dominance on the Indian Ocean eastern gyral current. *Geophysical Research Letters*, *40*(21), 5716–5721. https://doi.org/10.1002/2013GL057887

Menezes, V. V., Phillips, H. E., Vianna, M. L., & Bindoff, N. L. (2016). Interannual variability of the South Indian countercurrent. *Journal of Geophysical Research: Oceans*, *121*(5), 3465–3487. https://doi.org/10.1002/2015JC011417

Molinari, R. L., Olson, D., & Reverdin, G. (1990). Surface current distributions in the tropical Indian Ocean derived from compilations of surface buoy trajectories. *Journal of Geophysical Research: Oceans*, *95*(C5), 7217–7238. https://doi.org/10.1029/JC095iC05p07217

Momin, I. M., Mitra, A. K., Prakash, S., Mahapatra, D. K., Gera, A., & Rajagopal, E. N. (2015). Variability of sea surface salinity in the tropical Indian Ocean as inferred from Aquarius and in situ data sets. *International Journal of Remote Sensing*, *36*(7), 1907–1920. https://doi.org/10.1080/01431161.2015.1030045

Nonaka, M., & Sasaki, H. (2007). Formation mechanism for isopycnal temperature-salinity anomalies propagating from the eastern South Pacific to the equatorial region. *Journal of Climate*, *20*(7), 1305–1315. https://doi.org/10.1175/JCLI4065.1

Palastanga, V., van Leeuwen, P. J., Schouten, M. W., & de Ruijter, W. P. M. (2007). Flow structure and variability in the subtropical Indian Ocean: Instability of the South Indian Ocean countercurrent. *Journal of Geophysical Research: Oceans*, *112*(C1), C01001. https://doi.org/10.1029/2005JC003395

Peng, S., Qian, Y.-K., Lumpkin, R., Du, Y., Wang, D., & Li, P. (2015). Characteristics of the near-surface currents in the Indian Ocean as deduced from satellite-tracked surface drifters. Part I: Pseudo-Eulerian statistics. *Journal of Physical Oceanography*, *45*(2), 441–458. https://doi.org/10.1175/JPO-D-14-0050.1

Phillips, H. E., Tandon, A., Furue, R., Hood, R., Ummenhofer, C. C., Benthuysen, J. A., et al. (2021). Progress in understanding of Indian Ocean circulation, variability, air-sea exchange, and impacts on biogeochemistry. *Ocean Science*, *17*(6), 1677–1751. https://doi.org/10.5194/os-17-1677-2021

Qu, T., Lian, Z., Nie, X., & Wei, Z. (2019). Eddy-induced meridional salt flux and its impacts on the sea surface salinity maxima in the southern subtropical oceans. *Geophysical Research Letters*, *46*(20), 11292–11300. https://doi.org/10.1029/2019GL084807

Reid, J. L. (2003). On the total geostrophic circulation of the Indian Ocean: Flow patterns, tracers, and transports. *Progress in Oceanography*, *56*(1), 137–186. https://doi.org/10.1016/S0079-6611(02)00141-6

Roemmich, D., & Gilson, J. (2009). The 2004–2008 mean and annual cycle of temperature, salinity, and steric height in the global ocean from the Argo Program. *Progress in Oceanography*, *82*(2), 81–100. https://doi.org/10.1016/j.pocean.2009.1003.1004

Schanze, J. J., Schmitt, R. W., & Yu, L. L. (2010). The global oceanic freshwater cycle: A state-of-the-art quantification. *Journal of Marine Research*, *68*(3–1), 569–595. https://doi.org/10.1357/002224010794657164

Schmidtko, S., Johnson, G. C., & Lyman, J. M. (2013). MIMOC: A global monthly isopycnal upper-ocean climatology with mixed layers. *Journal of Geophysical Research: Oceans*, *118*(4), 1658–1672. https://doi.org/10.1002/jgrc.20122

Schmitt, R. W., & Blair, A. (2015). A river of salt. *Oceanography*, *28*(1), 40–45. https://doi.org/10.5670/oceanog.2015.04

Schott, F. A., Dengler, M., & Schoenefeldt, R. (2002). The shallow overturning circulation of the Indian Ocean. *Progress in Oceanography*, *53*(1), 57–103. https://doi.org/10.1016/S0079-6611(02)00039-3

Schott, F. A., Xie, S.-P., & McCreary, J. P., Jr. (2009). Indian Ocean circulation and climate variability. *Reviews of Geophysics*, *47*(1). https://doi.org/10.1029/2007RG000245

Siedler, G., Rouault, M., & Lutjeharms, J. R. E. (2006). Structure and origin of the subtropical South Indian Ocean countercurrent. *Geophysical Research Letters*, *33*(24), L24609. https://doi.org/10.1029/2006GL027399

Skofronick-Jackson, G., Petersen, W. A., Berg, W., Kidd, C., Stocker, E. F., Kirschbaum, D. B., et al. (2017). The Global Precipitation Measurement (GPM) mission for science and society. *Bulletin of the American Meteorological Society*, *98*(8), 1679–1695. https://doi.org/10.1175/BAMS-D-15-00306.1

Stramma, L., & Lutjeharms, J. R. E. (1997). The flow field of the subtropical gyre of the South Indian Ocean. *Journal of Geophysical Research: Oceans*, *102*(C3), 5513–5530. https://doi.org/10.1029/96JC03455

Terray, L., Corre, L., Cravatte, S., Delcroix, T., Reverdin, G., & Ribes, A. (2012). Near-surface salinity as nature's rain gauge to detect human influence on the tropical water cycle. *Journal of Climate*, *25*(3), 958–977. https://doi.org/10.1175/JCLI-D-10-05025.1

Vinogradova, N., Lee, T., Boutin, J., Drushka, K., Fournier, S., Sabia, R., et al. (2019). Satellite salinity observing system: Recent discoveries and the way forward. *Frontiers in Marine Science*, *6*, 243. https://doi.org/10.3389/fmars.2019.00243

Wang, Y., Li, Y., & Wei, C. (2020). Subtropical sea surface salinity maxima in the South Indian Ocean. *Journal of Oceanology and Limnology*, *38*(1), 16–29. https://doi.org/10.1007/s00343-019-8251-5

Worthington, L. (1976). On the North Atlantic circulation. *Johns Hopkins Oceanographic Studies*, *6*, 110.

Yu, L., Josey, S. A., Bingham, F. M., & Lee, T. (2020). Intensification of the global water cycle and evidence from ocean salinity: A synthesis review. *Annals of the New York Academy of Sciences*, *1472*(1), 76–94. https://doi.org/10.1111/nyas.14354

Yu, L., & Weller, R. A. (2007). Objectively analyzed air-sea heat fluxes for the global ice-free oceans (1981–2005). *Bulletin of the American Meteorological Society*, *88*(4), 527–540. https://doi.org/10.1175/BAMS-88-4-527

Zhang, L., & Qu, T. (2014). Low-frequency variability of South Pacific tropical water from Argo. *Geophysical Research Letters*, *41*(7), 2441–2446. https://doi.org/10.1002/2014GL059490

Zhang, N., Feng, M., Du, Y., Lan, J., & Wijffels, S. E. (2016). Seasonal and interannual variations of mixed layer salinity in the southeast tropical Indian Ocean. *Journal of Geophysical Research: Oceans*, *121*(7), 4716–4731. https://doi.org/10.1002/2016JC011854